J. Fluid Mech. (2014), *vol.* 757, *pp.* 747–769.
doi:10.1017/jfm.2014.486

Reynolds-number-dependent turbulent inertia and onset of log region in pipe flows

C. Chin[1], J. Philip[1,†], J. Klewicki[1,2], A. Ooi[1] and I. Marusic[1]

[1]Department of Mechanical Engineering, University of Melbourne, Parkville, VIC 3010, Australia

[2]Department of Mechanical Engineering, University of New Hampshire, Durham, NH 03824, USA

(Received 9 January 2014; revised 20 June 2014; accepted 19 August 2014;
first published online 26 September 2014)

A detailed analysis of the 'turbulent inertia' (TI) term (the wall-normal gradient of the Reynolds shear stress, $\mathrm{d}\langle -uv\rangle/\mathrm{d}y$), in the axial mean momentum equation is presented for turbulent pipe flows at friction Reynolds numbers $\delta^+ \approx 500$, 1000 and 2000 using direct numerical simulation. Two different decompositions for TI are employed to further understand the mean structure of wall turbulence. In the first, the TI term is decomposed into the sum of two velocity–vorticity correlations ($\langle v\omega_z\rangle + \langle -w\omega_y\rangle$) and their co-spectra, which we interpret as an advective transport (vorticity dispersion) contribution and a change-of-scale effect (associated with the mechanism of vorticity stretching and reorientation). In the second decomposition, TI is equivalently represented as the wall-normal gradient of the Reynolds shear stress co-spectra, which serves to clarify the accelerative or decelerative effects associated with turbulent motions at different scales. The results show that the inner-normalised position, y_m^+, where the TI profile crosses zero, as well as the beginning of the logarithmic region of the wall turbulent flows (where the viscous force is leading order) move outwards in unison with increasing Reynolds number as $y_m^+ \sim \sqrt{\delta^+}$ because the eddies located close to y_m^+ are influenced by large-scale accelerating motions of the type $\langle -w\omega_y\rangle$ related to the change-of-scale effect (due to vorticity stretching). These large-scale motions of $O(\delta^+)$ gain a spectrum of larger length scales with increasing δ^+ and are related to the emergence of a secondary peak in the $-uv$ co-spectra. With increasing Reynolds number, the influence of the $O(\delta^+)$ motions promotes viscosity to act over increasingly longer times, thereby increasing the y^+ extent over which the mean viscous force retains leading order. Furthermore, the TI decompositions show that the $\langle v\omega_z\rangle$ motions (advective transport and/or dispersion of vorticity) are the dominant mechanism in and above the log region, whereas $\langle -w\omega_y\rangle$ motions (vorticity stretching and/or reorientation) are most significant below the log region. The motions associated with $\langle -w\omega_y\rangle$ predominantly underlie accelerations, whereas $\langle v\omega_z\rangle$ primarily contribute to decelerations. Finally, a description of the structure of wall turbulence deduced from the present analysis and our physical interpretation is presented, and is shown to be consistent with previous flow visualisation studies.

Key words: pipe flow boundary layer, turbulence theory, turbulent flows

† Email address for correspondence: jimmyp@unimelb.edu.au

1. Introduction

This paper aims to further the mechanistic description of turbulent wall flows by clarifying the Reynolds-number-dependent properties and vorticity transport mechanisms that underlie the wall-normal gradient of the Reynolds shear stress. Since this gradient term derives from the time rate of change of momentum (i.e. inertial) part of the Reynolds-averaged Navier–Stokes equation, it is referred to here as the net mean effect of the turbulent inertia (TI), or simply 'TI' for short, and constitutes the dynamically most significant term in the mean momentum equation (cf. (1.3)).

Mechanistic depictions of wall-flow structure typically rely on collections of eddies of different sizes that deform and/or advect and interact with each other in varying ways (on average) for varying wall-normal positions. As extracted from numerical or experimental data, or proposed phenomenologically, coherent motion-based descriptions have long been utilised to concisely reflect our physical understanding of turbulent boundary layers (e.g. Perry & Chong 1982; Townsend 1987; Robinson 1991; Adrian 2007). A long-standing challenge, however, is connected to substantiating such descriptions from the equations of motion.

Herein, we start from the mean momentum equation for turbulent pipe flow, and decompose the TI term using two methods. (In both cases, the decomposed terms are further represented by their Fourier spectra.) The first method provides a means for understanding the advective transport and change-of-scale effect mechanisms associated with the TI, whereas the second quantifies the net accelerative effects due to turbulence at various length scales. In this regard, it is relevant to note that Bernard & Handler (1990) found that two fundamental mechanisms contribute to the Reynolds stress: one is due to the displacement of momentum-carrying fluid particles, and the other is a result of acceleration or deceleration of fluid particles. Both mechanisms are closely associated with the vortical motions in the flow.

The present analyses suggest a possible physical mechanism for the observation that the wall-normal location of the peak in the Reynolds shear stress moves outwards under inner normalisation with increasing Reynolds number (e.g. Sreenivasan 1989; DeGraaff & Eaton 2000; Wei *et al.* 2005; Buschmann, Indinger & Gad-el-Hak 2009), as well as the associated (and sometimes independently presented) finding that the wall-normal location of the beginning of the logarithmic region exhibits a dependence on the square root of the Reynolds number (e.g. Wei *et al.* 2005; Klewicki 2010; Marusic *et al.* 2013). Note that a Reynolds-number-dependent location for the onset of the log region is distinct from classical (two-layer) theory, i.e. what is usually presented in textbooks (e.g. Tennekes & Lumley 1972), which specifies that the log region begins at a fixed $O(\nu/u_\tau)$ location.

1.1. *Streamwise mean momentum balance*

The present study considers fully developed turbulent flow in a pipe. Before providing further motivation, we present the relevant mean equations of motion. Here the streamwise, radial and azimuthal directions are denoted as x, r and θ, with corresponding velocities represented as the sum of the mean and fluctuations, i.e. $U_x + u_x$, $U_r + u_r$ and $U_\theta + u_\theta$, and similarly for the pressure, $P + p$. The streamwise mean momentum equation for fully developed turbulent pipe flow is

$$0 = -\frac{1}{\rho}\frac{\partial P}{\partial x} + \frac{\nu}{r}\frac{\partial}{\partial r}\left(r\frac{\partial U_x}{\partial r}\right) - \frac{1}{r}\frac{\partial}{\partial r}(r\langle u_r u_x\rangle), \tag{1.1}$$

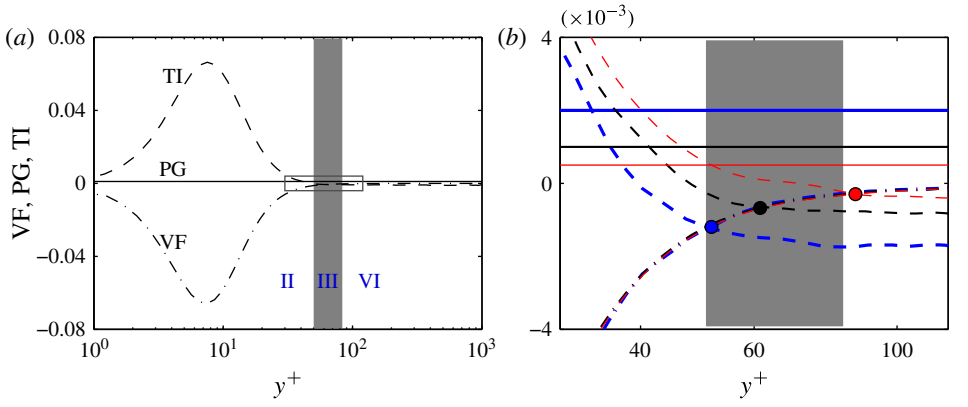

FIGURE 1. (Colour online) The three terms in (1.3). (*a*) For $\delta^+ \approx 1000$, showing the mean VF (dashed dotted line), mean effect of TI (dashed line) and PG (solid line). The grey region is the layer III where VF $\simeq$ TI $\simeq$ PG. (*b*) An expanded view of the rectangle in panel (*a*) encompassing layer III. Distributions for $\delta^+ \approx 500$ and 2000, in thick (blue) and thin (red) lines, respectively. The three dots are the location where VF = TI = $-$PG/2 (representing a central location within layer III) corresponding to the three δ^+.

where ν is the kinematic viscosity, ρ is the density and $\langle\ \rangle$ denotes ensemble-averaged quantities. With a constant pressure gradient (PG) (which is related to the wall shear stress, $\tau_w = -\rho\nu\, \mathrm{d}U_x/\mathrm{d}r|_w$), (1.1) can be written as (see e.g. Tennekes & Lumley 1972)

$$0 = \frac{1}{\delta}\frac{\tau_w}{\rho} + \nu\frac{\partial^2 U_x}{\partial r^2} + \frac{\partial(-\langle u_x u_r\rangle)}{\partial r}. \tag{1.2}$$

We define the wall-normal coordinate $y = \delta - r$ and the respective velocities $U = U_x$, $V = -U_r$ and $W = -U_\theta$ with the corresponding fluctuating components, $u = u_x$, $v = -u_r$ and $w = -u_\theta$. (Note that in the wall-normal system the direction of the angular coordinate and the corresponding velocity have to reverse directions to keep the coordinate system right-handed.) Superscript '+' denotes inner normalisation, i.e. scaling with the viscous length and velocity scales, ν/U_τ and U_τ, respectively, where $U_\tau = \sqrt{\tau_w/\rho}$ is the friction velocity. Rewriting (1.2) in terms of a coordinate system fixed to the pipe wall and inner normalising yields the equation for the mean momentum balance,

$$0 = \underbrace{\frac{\mathrm{d}\langle -uv\rangle^+}{\mathrm{d}y^+}}_{\text{TI}} + \underbrace{\frac{\mathrm{d}^2 U^+}{\mathrm{d}y^{+2}}}_{\text{VF}} + \underbrace{\frac{1}{\delta^+}}_{\text{PG}}. \tag{1.3}$$

The first term on the right-hand side of (1.3) is the time-averaged effect of the turbulent inertia, TI, while the second and the third terms are the mean viscous force (VF) and mean pressure gradient, PG, respectively. The corresponding equation for turbulent channel flows has the same form as (1.3), whereas for a turbulent boundary layer the PG term is replaced by the mean inertia term, which in order of magnitude is similar to that of the PG term. These observations imply that the results herein also have relevance to turbulent channel flow, and in large part to boundary layers as well.

Figure 1(*a*) shows the terms in (1.3) at δ^+ $(= \delta U_\tau/\nu) \approx 1000$. Following Wei *et al.* (2005), we consider four regions, depending on the leading-order balance between the terms in (1.3). Region II is where TI $\simeq$ VF, region III is where all the terms in (1.3) are of the same order (shown in filled grey colour), and region IV is the

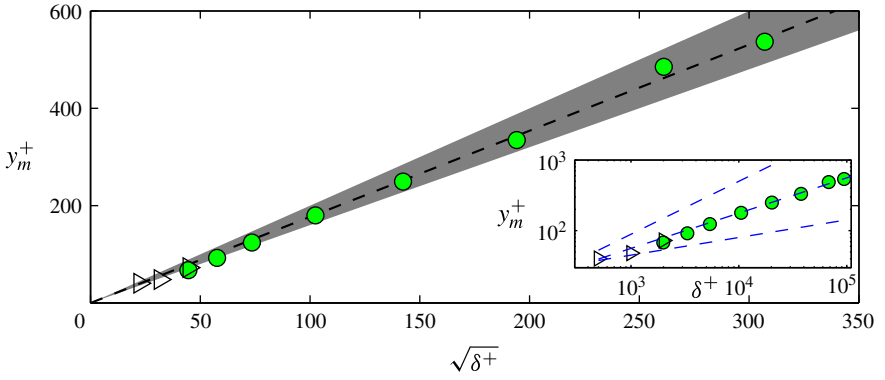

FIGURE 2. (Colour online) Peak location of the Reynolds shear stress ($\langle -uv\rangle^+$), y_m^+ or the zero crossing of TI as a function of $\sqrt{\delta^+}$. The open triangles are from the DNS database used in this paper, whereas the filled circles correspond to the shear stress calculated from the mean velocity profile of the smooth 'superpipe' data of Hultmark *et al.* (2013) using (1.3). The dashed black line is a least-squares fit of all the data, $y_m^+ = 1.77\sqrt{\delta^+}$, and the shaded region is between the lines $y_m^+ = 1.6\sqrt{\delta^+}$ and $2.0\sqrt{\delta^+}$. The inset shows the same data on a log–log scale with y_m^+ versus δ^+, and the three dashed (blue) lines have slopes 3/4, 1/2 and 1/4 from top to bottom.

inertial region where TI $\simeq$ PG. (Note that region I, where PG $\simeq$ VF, is very close to the wall and not depicted in figure 1.) The end of region III (or the beginning of region IV) is the beginning of the log region where the VF term loses leading order (e.g. Wei *et al.* 2005; Klewicki 2013*b*). The location of layer III is enclosed in figure 1(*a*) by a rectangle, which is again shown in figure 1(*b*) along with data from $\delta^+ \approx 500$ and 2000. The location surrounding layer III (approximately centred on the dots that denote the position where VF = TI = -0.5PG) is clearly seen to be moving to larger y^+ with increasing δ^+.

Notice that the effect of turbulence in the mean momentum equation is explicitly contained in the TI term. In the near-wall region, TI acts like a momentum source (a positive TI) that is counterbalanced by the mean VF. Away from the wall, the TI motions act as a sink of momentum (a negative TI) to counterbalance the momentum being input by the mean PG (Klewicki *et al.* 2007; Eyink 2008).

Overall, momentum transport in turbulent wall flows is largely dictated by the mechanical stirring associated with inertia of the turbulent eddies. As made apparent by the above discussion, this effect is embodied in the TI term of (1.3). Owing to this, the overarching first aim of this investigation is to characterise the effects of Reynolds-number variation on the TI, and to clarify the resulting consequences relative to the structure of (1.3). As described above, attaining this goal is fostered by decomposing the TI term into two different (albeit equally valid) spectral decompositions. A central issue relating to Reynolds-number dependence is the position of layer III, which, by its definition, always contains y_m^+, the location of the zero crossing of TI (or the peak location of $-\langle uv\rangle^+$) and across which the VF term in (1.3) loses leading-order importance. This behaviour is now briefly discussed.

1.2. *Wall-normal location of the peak in Reynolds shear stress*

Figure 2 shows y_m^+ as a function of $\sqrt{\delta^+}$ over the range $500 \lesssim \delta^+ \lesssim 100\,000$. The high-Reynolds-number y_m^+ data of figure 2 (filled circles) are determined by employing

the once-integrated form of (1.3) in combination with the (second-order-accurate) numerically differentiated mean velocity profiles of Hultmark *et al.* (2013). Along with the inset (which helps to compare the various power-law behaviours of y_m^+), the figure clearly supports $y_m^+ \sim \sqrt{\delta^+}$ scaling. The y_m^+ scaling is already known both empirically and analytically (e.g. Sreenivasan 1989; Sreenivasan & Sahay 1997; Wei *et al.* 2005; Buschmann *et al.* 2009; Klewicki 2010), and figure 2 supports this finding with new direct numerical simulation (DNS) and high δ^+ experimental data.

Note that the classical two-layer description of the turbulent boundary layer might seem to 'predict' the $\sqrt{\delta^+}$ scaling of y_m^+. This is usually obtained by substituting the log-law distribution of U^+ into the mean momentum equation (1.3), and substituting $\mathrm{d}\langle -uv\rangle^+/\mathrm{d}y^+ = 0$. There are at least two serious problems with this approach. (i) With reference to figure 1, it is shown that the zero crossing of TI (or the location of the peak in the Reynolds shear stress distribution, y_m^+) is 'below' layer IV or the inertial/log region, and not 'inside' the log region (since VF is still of importance at y_m^+, unlike in layer IV, where VF loses its dominance), and the two-layer 'prediction' of y_m^+ assumes y_m^+ to be inside the log region, which is not correct. (ii) The classical theory first finds the solution for $U^+(y^+)$, the log law, when both $U^+(y^+)$ and $\langle -uv\rangle^+$ are unknowns in a single unclosed mean momentum equation, whereas in the determination of the logarithmic law for the mean velocity from the theory described in Fife, Klewicki & Wei (2009), both $U^+(y^+)$ and $\langle -uv\rangle^+$ are simultaneously determined, as they must be since they are the unknowns in the mean momentum equation (1.3).

The outward movement of $y_m^+ \sim \sqrt{\delta^+}$ is directly associated with the outward movement of layer III, and, along with the fact that the width of layer III is $\approx 1.0\sqrt{\delta^+}$ (see Wei *et al.* (2005) for an analytical description and experimental evidence), shows that the beginning of layer VI or the lower bound of the logarithmic region moves outwards like $\sqrt{\delta^+}$ (e.g. Afzal 1982; Wei *et al.* 2005; Klewicki 2013*b*). This Reynolds-number dependence is seen empirically in both the mean streamwise velocity profiles and the streamwise turbulence intensity profiles for both pipes and boundary layers (Marusic *et al.* 2013). The detailed physical mechanisms that give rise to this behaviour are, however, not known.

Our second more specific aim is to present a plausible explanation of this movement of the beginning of the log region (in viscous scaling) with Reynolds number (and the corresponding scaling of y_m^+) using the spectral decomposition described in § 2.

1.3. *Organisation of the rest of the paper*

The rest of the paper is organised as follows. Section 2 presents the two types of decompositions and their spectral representations that will be used throughout this paper. Section 3 presents the primary results from the decompositions and provides some physical interpretations of these results. The decompositions are also analysed in terms of the large- and small-scale contributions, the results of which have implications regarding the onset of the logarithmic region. In § 4 we summarise the main results from the analyses, and subsequently present further interpretations regarding the underlying physical mechanisms.

2. Decomposition of the turbulent inertia term

The TI term is decomposed into two different forms to aid in educing the flow physics. Although only sparingly employed, owing to the inherent measurement

challenges, these decompositions have been explored previously by Klewicki (1989), Guala, Hommema & Adrian (2006), Balakumar & Adrian (2007) and Morrill-Winter & Klewicki (2013). These two decompositions have, however, never previously been employed in concert. As will become apparent, this significantly clarifies the relevant flow physics.

The first decomposition is

$$\frac{\partial \langle -uv \rangle^+}{\partial y^+} = \langle v\omega_z \rangle^+ + \langle -w\omega_y \rangle^+, \tag{2.1}$$

which holds for a streamwise-independent mean quantity (Tennekes & Lumley 1972). The relevant vorticity ($\omega = \boldsymbol{\nabla} \times \boldsymbol{u}$) component fluctuations are $-\omega_z = \omega_\theta = \partial u_r/\partial x - \partial u_x/\partial r$ and $-\omega_y = \omega_r = (1/r)\,\partial u_x/\partial\theta - \partial u_\theta/\partial x$.

A physical interpretation of the two terms on the right-hand side in (2.1) (consistent with Taylor (1932), Tennekes & Lumley (1972) and Klewicki (1989)) aids in forming a mechanistic view of wall-bounded turbulent flows from the data. In his vorticity transport theory, Taylor (1932) considered $\langle v\omega_z \rangle$ and interpreted it in terms of gradient transport. Tennekes & Lumley (1972) applied scaling arguments to $\langle -uv \rangle \sim u^* l\, \partial U/\partial y$ by employing a generic mixing length representation, where u^* is a characteristic constant velocity and $l(y)$ is a length scale that depends on wall normal position (the usual case for wall-bounded turbulent flows). Here, we note that for a generic turbulent flow a mixing-length-based description is inadequate. In the context of wall-bounded turbulence, however, these arguments have use in qualitatively describing the scaling of the terms in (2.1). Considering this, the TI term is seen to scale as $-(u^* l\, \partial \Omega_z/\partial y) - (u^* \Omega_z\, \partial l/\partial y)$, where $\Omega_z = -\partial U/\partial y$.

The term $\langle v\omega_z \rangle^+$ $(=\langle u_r \omega_\theta \rangle^+)$, the first term on the right-hand side of (2.1), represents the mean effect of motions bearing spanwise vorticity being advected by the wall-normal velocity fluctuations. Following Morrill-Winter & Klewicki (2013), this mechanism is herein called 'vorticity dispersion' (or advection of vorticity). The second term corresponds to $\langle -w\omega_y \rangle^+$ $(=\langle -u_\theta \omega_r \rangle^+)$, and may be interpreted as a body force associated with the change of scale of eddies in a flow field of varying length scale $(\partial l/\partial y)$, called the 'vorticity-stretching inertial force' (Tennekes & Lumley 1972). Note that, strictly, 'vortex stretching' has a form of strain rate operating on a component of vorticity (e.g. Tennekes & Lumley 1972, p. 83). However, in the case of wall-bounded turbulent flows, consistent with the scaling arguments of Tennekes & Lumley (1972, pp. 80, 85), the analysis of the vorticity transport equation and mean enstrophy equation by Klewicki (2013*a*) reveals that $\langle -w\omega_y \rangle^+$ has an effect that is associated with the physical mechanism of vorticity stretching and reorientation.

The $\langle v\omega_z \rangle^+$ and $\langle -w\omega_y \rangle^+$ contributions can further be decomposed into their respective co-spectra. This allows analysis of the contributions from different streamwise wavelengths (λ_x^+). Thus,

$$\left.\begin{aligned} \langle v\omega_z \rangle^+ &= \int_0^\infty \Phi^+_{v\omega_z}\, \mathrm{d}\log(\lambda_x^+), \\ \langle -w\omega_y \rangle^+ &= \int_0^\infty \Phi^+_{-w\omega_y}\, \mathrm{d}\log(\lambda_x^+), \end{aligned}\right\} \tag{2.2}$$

where $\Phi^+_{v\omega_z} = k_x \phi^+_{v\omega_z}$ is the premultiplied co-spectrum of v and ω_z, k_x is the streamwise wavenumber, and a similar definition holds for $\Phi^+_{-w\omega_y}$.

The representation of the correlations in terms of their spectral content allows the contributions to TI to be characterised relative to their scale. Apart from

δ^+	L_x/δ	Δx^+	$\Delta y^+\|_{wall}$	$\Delta r\theta^+\|_{wall}$	TU_b/L_x
500	20π	6.83	0.070	8.2	22
1002	8π	7.87	0.033	6.6	12
2003	3π	9.22	0.024	7.6	6

TABLE 1. DNS computational parameters. Here, L_x is the computational domain length; Δx^+, Δy^+ and $\Delta r\theta^+$ correspond to the streamwise, radial and azimuthal grid resolutions; and TU_b/L_x is the wash-through time based on bulk velocity U_b and domain length L_x where the statistics are averaged.

the well-known near-wall streaks that are ∼1000 viscous scales long and spaced ∼100 viscous scales wide (e.g. Kline *et al.* 1967; Robinson 1991), the existence of large-scale motion (LSM) having a streamwise extent of 2δ–3δ has been documented in boundary layers, pipes and channels (e.g. Kim & Adrian 1999; Adrian, Meinhart & Tomkins 2000; Marusic 2001; Balakumar & Adrian 2007; Dennis & Nickels 2011). There also exists very-large-scale motion (VLSM) in pipes and channels whose lengths are in excess of 10δ (Monty *et al.* 2007; Lee & Sung 2013) and similarly superstructures in boundary layers (Hutchins & Marusic 2007). These LSM and VLSM have been evidenced to modulate the small scales in layer II (Mathis *et al.* 2009; Marusic, Mathis & Hutchins 2010) and contribute to an increasing fraction of the total turbulence kinetic energy with increasing δ^+.

The second decomposition of TI is given by the integral of the derivative of the co-spectrum of u and v,

$$\frac{\partial\langle -uv\rangle^+}{\partial y^+} = \int_0^\infty \frac{\partial \Phi^+_{-uv}}{\partial y^+}\,\mathrm{d}\log(\lambda_x^+), \tag{2.3}$$

which can be written as contributions from small and large scales:

$$\frac{\partial\langle -uv\rangle^+}{\partial y^+} = \left[\int_0^{\lambda_c^+} \frac{\partial \Phi^+_{-uv}}{\partial y^+}\,\mathrm{d}\log(\lambda_x^+)\right]_{\mathrm{SS}} + \left[\int_{\lambda_c^+}^\infty \frac{\partial \Phi^+_{-uv}}{\partial y^+}\,\mathrm{d}\log(\lambda_x^+)\right]_{\mathrm{LS}}. \tag{2.4}$$

In (2.4), SS and LS correspond to cut-off wavelengths at the small scales and the large scales, respectively. The values of the cut-off wavelengths employed herein are specified later. Equation (2.3) is interpreted as the net turbulent force spectra by Guala *et al.* (2006) (since TI is part of the mean momentum balance or the streamwise force balance), whereby positive contributions are associated with accelerations and negative contributions are associated with decelerations.

3. Results and discussion

Data from DNS by Chin *et al.* (2010) and Chin, Monty & Ooi (2014) are used to carry out an analysis of the TI term in (1.3). The Reynolds number ranges from $\delta^+ \approx 500$ to 2000. A summary of the DNS datasets is shown in table 1. More details regarding the simulations can be found in Chin *et al.* (2010, 2014).

Figure 3(*a*,*b*) shows the variation of Reynolds stress and its wall-normal gradient with wall-normal location (y^+) for three different δ^+. The peak value of $\langle -uv\rangle^+$ increases correspondingly with δ^+, and is attained on an increasingly broad plateau

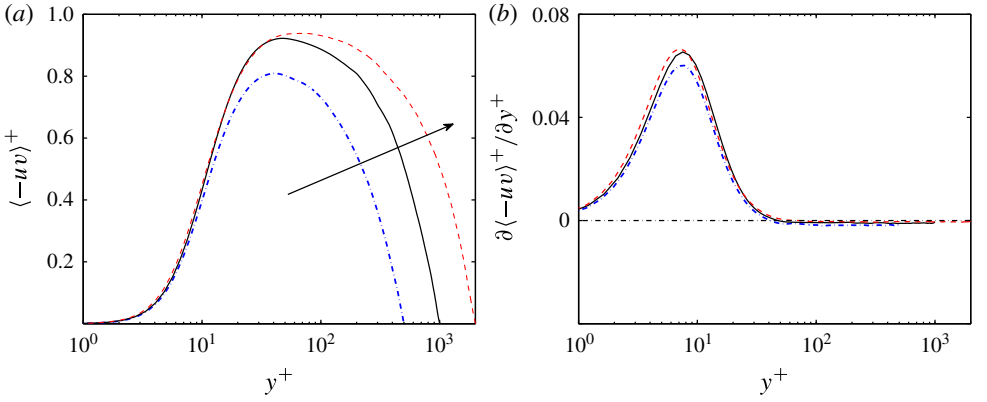

FIGURE 3. (Colour online) Reynolds-number effect on (*a*) the Reynolds stress $\langle -uv \rangle^+$ and (*b*) the TI ($\partial \langle -uv \rangle^+ / \partial y^+$). The arrow in (*a*) denotes increasing Reynolds numbers, with $\delta^+ \approx 500$ (blue dot-dashed line), 1000 (black solid line) and 2000 (red dashed line).

with increasing δ^+, as described by Sreenivasan & Sahay (1997). The value of y_m^+ increases with δ^+ and is observed to increase like $\sqrt{\delta^+}$, as presented in figure 2, and in agreement with a number of previous analyses and measurements (e.g. Afzal 1982; Sreenivasan & Sahay 1997; Abe, Kawamura & Matsuo 2001; Wei *et al.* 2005; Buschmann *et al.* 2009; Klewicki *et al.* 2012).

3.1. *Velocity–vorticity decomposition*

The TI term is decomposed into a velocity–vorticity form according to (2.1), and the wall-normal variations of each correlation are shown in figure 4(*a*,*b*) for $\delta^+ \approx 500$, 1000 and 2000 (and the inset shows a zoomed-in view of a portion of the distribution). Note that the relationship between figures 3(*b*) and 4(*a*,*b*) is given by (2.1). Figure 4(*a*) presents the $\langle v\omega_z \rangle^+$ term, which appears to remain nearly invariant over the given Reynolds-number range. The $\langle -w\omega_y \rangle^+$ term in figure 4(*b*) exhibits more readily noticeable changes under inner normalisation with increasing δ^+. The contributions from $\langle v\omega_z \rangle^+$ and $\langle -w\omega_y \rangle^+$ to the TI vary with y^+ and δ^+. Their relative contributions to TI are clarified by taking the ratio of $\langle v\omega_z \rangle^+$ and $\langle w\omega_y \rangle^+$, as shown in figure 5(*a*). From (2.1), it is apparent that this ratio must pass through unity at y_m^+. Figure 5(*b*) is a zoomed-in view of the region surrounding y_m^+. Beyond y_m^+, the $\langle v\omega_z \rangle^+$ term becomes larger than the $\langle -w\omega_y \rangle^+$ term.

Given the information in figures 2, 3 and 5, we now use figure 4 to clarify which scales are responsible for the increase in the $\langle -w\omega_y \rangle^+$ contribution with δ^+ in the region interior to y_m^+. Spectra of $\langle v\omega_z \rangle^+$ and $\langle -w\omega_y \rangle^+$ (figure 4*c*–*h*, left and right column, respectively) reveal the underlying scale contributions according to the decomposition of (2.2). In pre-multiplied form, the area under the spectrogram quantifies the contribution to the correlation. Almost independent of Reynolds number, the $\langle v\omega_z \rangle^+$ co-spectra seem to be relatively fixed. Conversely, the $\langle -w\omega_y \rangle^+$ term, however, exhibits much more apparent changes in scale with δ^+. Note further that we have plotted a dashed line at $y^+ = y_m^+$ in figure 4(*d*,*f*,*h*), denoting where the peak of $\langle -uv \rangle^+$ occurs, or equivalently where the TI term passes through zero. These spectra indicate that the $\langle -w\omega_y \rangle^+$ contributions vary with δ^+ primarily at wavelengths that are $O(\delta^+)$, and these variations are primarily about the wall-normal location of $y^+ = y_m^+$.

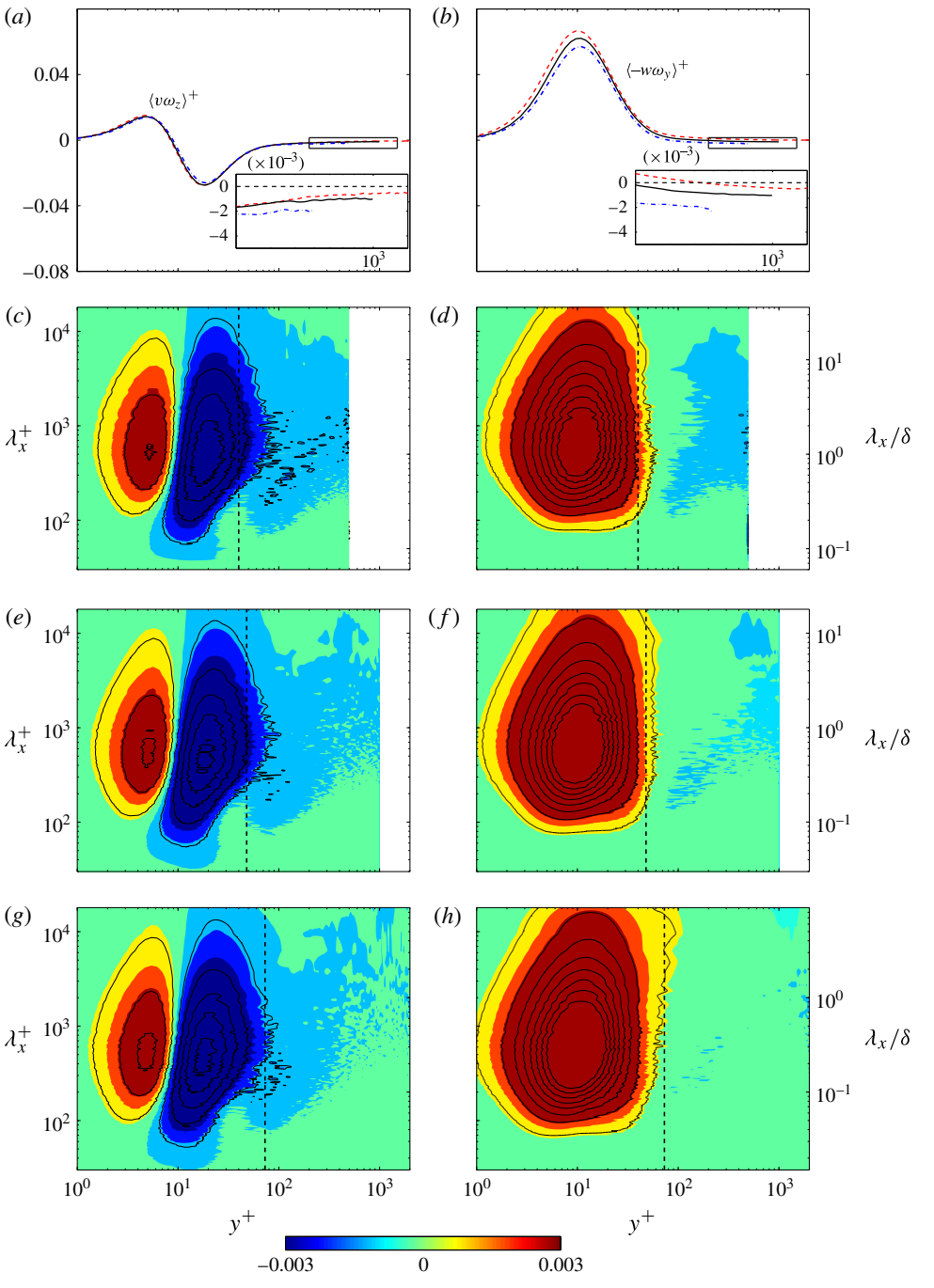

FIGURE 4. (Colour online) Decomposition of (*a*) $\langle v\omega_z\rangle^+$ into ((*c*) $\delta^+ \approx 500$, (*e*) $\delta^+ \approx 1000$ and (*g*) $\delta^+ \approx 2000$), the co-spectra of v and ω_z, $\Phi_{v\omega_z}$. Decomposition of (*b*) $\langle -w\omega_y\rangle^+$ into ((*d*) $\delta^+ \approx 500$, (*f*) $\delta^+ \approx 1000$ and (*h*) $\delta^+ \approx 2000$), the co-spectra of $-w$ and ω_y, $\Phi_{-w\omega_y}$. Line styles in (*a*) and (*b*) are as in figure 3. Colour map goes from −0.003 (blue) to 0.003 (red). The black dashed line is at $y^+ = y_m^+$. The insets in (*a*) and (*b*) are zoomed-in views of the portion of the distribution showing their variation close to the zero line. Contour level begins at −0.009 with increments of 0.002.

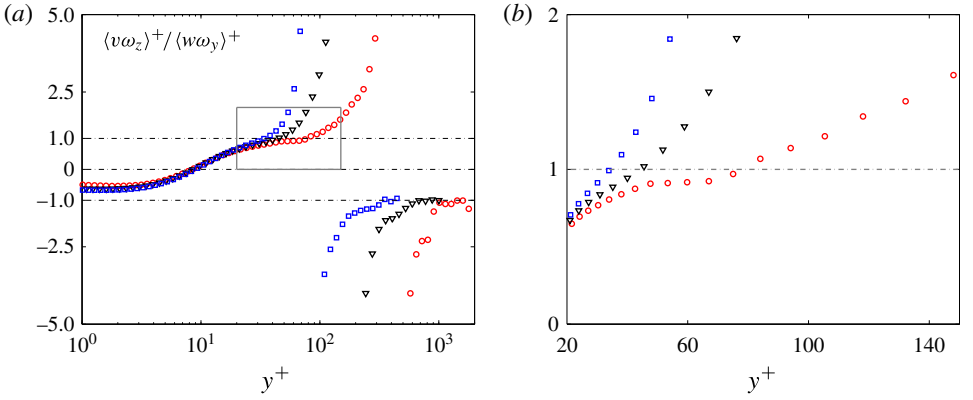

FIGURE 5. (Colour online) (*a*) Comparison of the ratios of $\langle v\omega_z\rangle^+$ and $\langle w\omega_y\rangle^+$ for different Reynolds numbers $\delta^+ \approx 500$ (blue squares), 1000 (black triangles) and 2000 (red circles). (*b*) Zoomed-in region within the enclosed grey lines.

This observation is consistent with previous findings that the large-scale motions (residing beyond y_m^+) modulate the near-wall flow (Marusic *et al.* 2010), and in doing so influence the near-wall vorticity redistribution processes (Morrill-Winter & Klewicki 2013), as well as possibly increasing the streamwise length of the vortices near the wall with increasing Reynolds number (Wei & Willmarth 1989).

The $\langle -w\omega_y\rangle^+$ term provides the dominant positive contribution to the TI term over the domain close to the wall. On the other hand, $\langle v\omega_z\rangle^+$ changes sign close to the wall, going from positive very close to the wall to negative a little farther from the wall, as observed in the left column of figure 4. To investigate this further, we consider the joint probability density function (p.d.f.) of v and ω_z at $y^+ \approx 5$, where $\langle v\omega_z\rangle^+$ is strongly positive. This joint p.d.f., at $\delta^+ = 1000$, is presented in figure 6(*a*). The thinner upper panel shows the p.d.f. of ω_z and the thinner right panel displays the p.d.f. of v. From the distribution of the joint p.d.f. of v and ω_z, it is unclear which quadrant is dominant. To clarify this, figure 7(*a*) shows the weighted joint p.d.f. of $v\omega_z$, which is obtained by multiplying the joint p.d.f. contribution (figure 6*a*) by the $v\omega_z$ value at each v and ω_z. The weighted joint p.d.f. is shown as a percentage contribution of the total $\langle v\omega_z\rangle^+$. The contour lines begin at 0.015 with increments of 0.015. The results in figure 7(*a*) show that the first quadrant dominates, with a 47 % contribution. This is consistent with the vertical advection of sublayer streaks, which comprise positive ω_z (because the mean spanwise vorticity has a magnitude that is large compared to the fluctuations at these y^+ locations very close to the wall) and are carried upwards by the vertical velocity (Klewicki, Murray & Falco 1995). A similar analysis is performed at $y^+ \approx 18$. This wall-normal location is where $\langle v\omega_z\rangle^+$ attains its largest negative value (see figure 4*a*). Here the second quadrant is seen to be predominant, contributing 38 % to the overall $\langle v\omega_z\rangle^+$, whereas the fourth quadrant contributes 28 %. Second-quadrant motions are interpreted as comprising clockwise-rotating vortical motions that are translating away from the wall (Klewicki *et al.* 1995; Klewicki & Hirschi 2004). This can be viewed as the heads of the hairpin vortices that detach from the sheet-like sublayer vorticity field and advect outwards, as incorporated in a variety of physical models (e.g. Perry & Chong 1982; Wallace 1982; Zhou *et al.* 1999; Adrian *et al.* 2000).

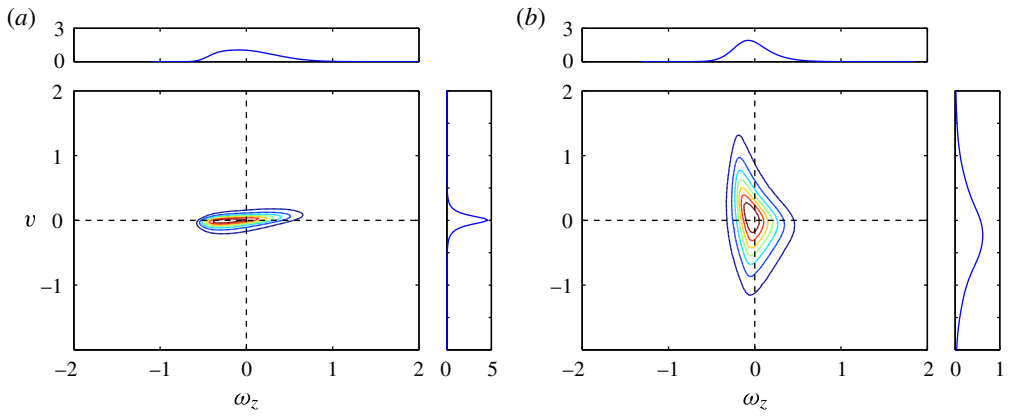

FIGURE 6. (Colour online) Joint p.d.f. of $(v\omega_z)$ at wall-normal location (*a*) $y^+ = 5$ and (*b*) $y^+ = 18$ for $\delta^+ \approx 1000$. The thinner upper panel shows the p.d.f. of ω_z and the thinner right panel shows the p.d.f. of v.

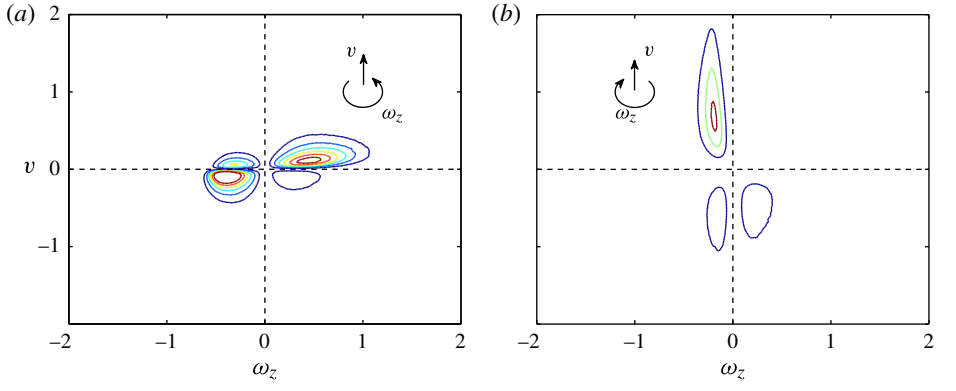

FIGURE 7. (Colour online) Weighted joint p.d.f. of $v\omega_z$ at wall-normal location (*a*) $y^+ = 5$ and (*b*) $y^+ = 18$ for $\delta^+ \approx 1000$. Contours begin at 0.015, with increments of 0.015.

3.2. *Force spectrum decomposition*

Spectrograms of the co-spectra Φ^+_{-uv} for DNS channel flow at $\delta^+ \approx 550$ and 950 have previously been presented by del Álamo & Jiménez (2003) and del Álamo *et al.* (2004), as well as in pipe flow DNS by Wu, Baltzer & Adrian (2012) at $\delta^+ \approx 685$. Wu *et al.* (2012) employed a perspective that focused on describing the net turbulent force. Here we focus on developing a physical understanding of the kinds of vortical motions that contribute to the TI term. Reynolds-number effects on Φ^+_{-uv} have previously been studied experimentally by Guala *et al.* (2006) and Balakumar & Adrian (2007). The experimental measurements by Balakumar & Adrian (2007) are, however, taken at limited wall-normal locations between $0.05 < y/\delta < 1$, with their nearest wall measurement being $y^+ \approx 64$ at $\delta^+ \approx 531$.

The pre-multiplied co-spectrum of the Reynolds stress, Φ^+_{-uv}, is shown in the left column of figure 8, and its derivative, $\partial\Phi^+_{-uv}/\partial y^+$, is displayed on the right of figure 8 for $\delta^+ \approx 500$, 1000 and 2000 in panels (*b*), (*d*) and (*f*), respectively. The right column of figure 8 can also be obtained by adding the co-spectra of $\langle v\omega_z\rangle^+$

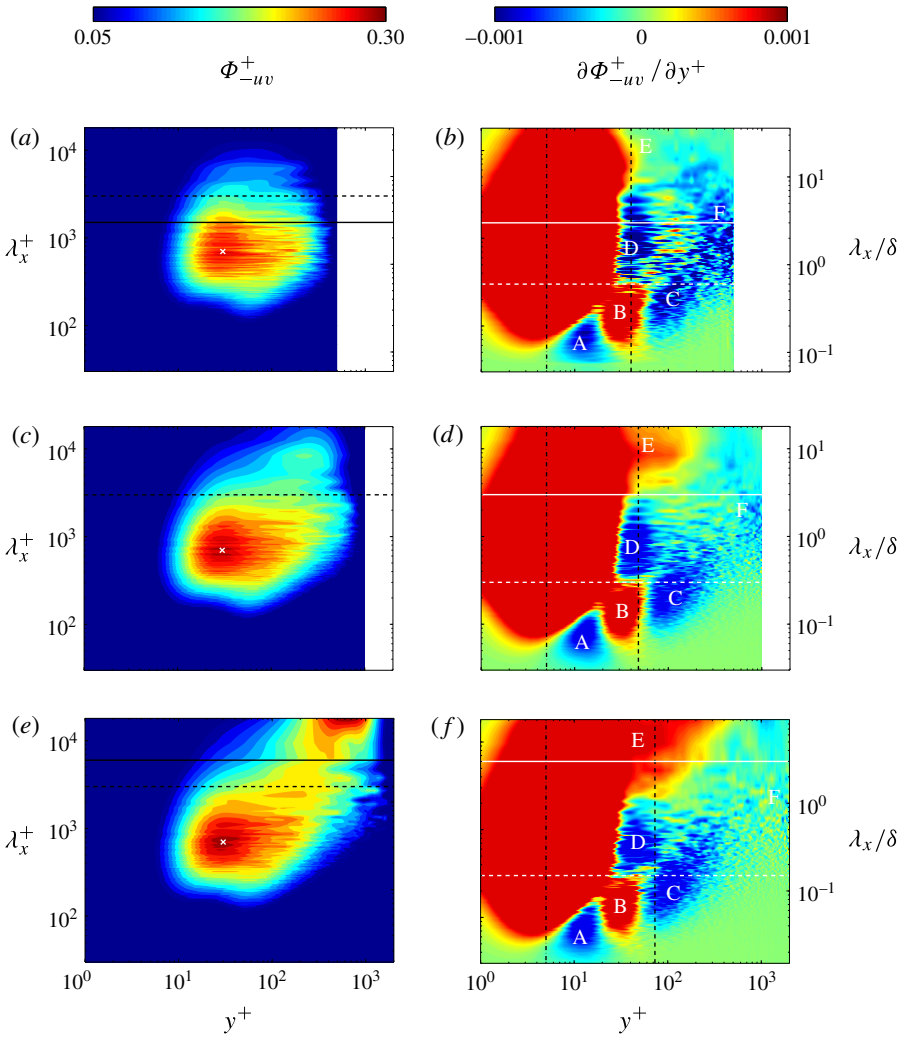

FIGURE 8. (Colour online) Co-spectra for increasing Reynolds number for $\delta^+ \approx 500$, 1000 and 2000 from top to bottom. Left column for the co-spectra of Reynolds stress Φ^+_{-uv}. The white '×' denotes the inner peak location at $y^+ \approx 30$, $\lambda_x^+ \approx 700$. Right column for the co-spectra of $\partial\Phi^+_{-uv}/\partial y^+$. In the left column, the black dashed line is at $\lambda_x^+ = 3000$ and the black solid line corresponds to $\lambda_x^+ = 3\delta^+$. Note that, for $\delta^+ \approx 1000$, $\lambda_x^+ = 3\delta^+ = 3000$. In the right column, the black dashed line is at $y^+ = y_m^+$ and the black dot-dashed line is at $y^+ = 5$. The white dashed line is at $\lambda_x^+ = 300$ and white solid line is at $\lambda_x/\delta = 3$.

(figure 4, left column) and $\langle -w\omega_y \rangle^+$ (figure 4, right column). The positive (red) regions contribute to acceleration and the negative (blue) regions to deceleration. The left column of figure 8 clearly shows the effect of Reynolds number on the co-spectra of uv. These results provide evidence that a secondary peak emerges with increasing δ^+. This conclusion, however, is somewhat tempered by the length of the computational domain at the highest δ^+ being a little smaller than desired. It is interesting to note that the location of the inner peak (denoted by the white '×' on the figure) appears essentially invariant (at $y^+ \approx 30$ and $\lambda_x^+ \approx 700$) for varying δ^+.

The wall-normal derivative of Φ^+_{-uv} is shown in the right column of figure 8 with increasing Reynolds number. The colour map ranges from -0.001 (blue) to 0.001 (red). From the spectrogram, one can easily identify the contributions from different length scales to the overall flow. Blue corresponds to momentum sink-like contributions, and red to momentum source-like contributions. In the viscous sublayer (denoted by a vertical black dot-dashed line), the results for all three Reynolds numbers are similar, consisting of a strong momentum source over the entire wavelength domain.

Note that in their force spectrum analysis of pipe flow at a fixed $\delta^+ = 685$, Wu *et al.* (2012) identified three spectral ranges in wavelength space to understand the acceleration or deceleration caused by different scales of motion. The first range includes wavelengths up to 0.5δ, which they called the 'main turbulent motions'. The next range is associated with the LSM and extends from 0.5δ to 3δ. The third range extends beyond 3δ, which they identify as the VLSM. The white horizontal dashed and solid lines in figure 8 (right column) correspond to $\lambda_x^+ = 300$ and $\lambda_x = 3\delta$, respectively. The figures also show several regions marked with letters A to E corresponding to regions of approximately constant spectral intensity (acceleration and deceleration in shades of red and blue, respectively). The relative movement of the solid horizontal (white) lines and these constant force regions suggests that Reynolds-number variations cause non-trivial changes in normalised size of the underlying coherent motions. The regions below the $\lambda_x^+ \approx 300$ (A, B and C) line, however, seem fixed with δ^+, even though other regions depend on δ^+. In what follows, we analyse each region separately.

An immediately noticeable feature is the small island (region A) of negative contribution. This region is approximately located between $5 < y^+ < 20$ and $\lambda_x^+ < 120$ and is present for all Reynolds numbers shown here. The mechanism behind the occurrence of momentum sink A can be identified from the decomposition of TI into $\langle -w\omega_y \rangle$ and $\langle v\omega_z \rangle^+$ terms shown in figure 4. This is clarified in figure 4(*c*,*e*,*g*) and (*d*,*f*,*h*) by focusing on the region $5 < y^+ < 20$ and $\lambda_x^+ < 120$. Here it is seen that region A mainly derives from the negative co-spectrum of $v\omega_z$. This negative co-spectrum has to be due to either v or ω_z being negative, but not both. The analysis in § 3.1 (cf. figure 7*b*), however, suggests that region A is primarily due to positive v and negative ω_z, i.e. clockwise spanwise vortical motions being advected upwards by the wall-normal velocity (consistent with the lifting head of a hairpin-like vortex).

Region B shows a small momentum source zone, also seen previously by Balakumar & Adrian (2007) and Wu *et al.* (2012). The present results suggest that region B remains essentially invariant with Reynolds number. The origin of this isolated acceleration can be discerned from figure 4. In figure 4(*c*,*e*,*g*), the (y^+, λ^+) region B is a weak momentum source. More significantly, the $\langle -w\omega_y \rangle^+$ term (figure 4*d*,*f*,*h*), exhibits a clear momentum source zone in the same (y^+, λ^+) domain of B. When both of the velocity–vorticity contributions are combined, one observes the manifestation of flow acceleration as shown in region B in figure 8.

Regions C and D are also momentum sink zones, their nature, however, being different from that of region A. Region A solely derives from the $v\omega_z$ contribution, since the $w\omega_y$ co-spectrum is essentially zero over the relevant λ^+ range. On the other hand, region C is positioned at a y^+ position beyond which the co-spectrum of $w\omega_y$ is non-zero, while D seems to have the most complexity, as it results from a non-trivial difference between $v\omega_z$ and $w\omega_y$ co-spectra. Here we note that C seems invariant, whereas D seems to focus around a narrowing wavelength range with increasing δ^+. The wavelengths that bound D range from $\lambda_x^+ \approx 300$ (constant for all δ^+) to

$\lambda_x^+ \approx 8\delta^+$ ($\delta^+ \approx 500$), $4\delta^+$ ($\delta^+ \approx 1000$) and $1.5\delta^+$ ($\delta^+ \approx 2000$). This bounding limit differs from that reported by Wu *et al.* (2012) of 0.5δ–3δ. This could be reasoned by the difference in Reynolds number and the effects of LSM and VLSM at higher Reynolds numbers.

From figure 8, there is evidence that the reduction of the bounding wavelength limit of D is due to the presence of a momentum source region E, which spans a greater (y^+, λ^+) domain with increasing Reynolds number. Guala *et al.* (2006) and Balakumar & Adrian (2007) have shown that, within the logarithmic region, the VLSM is associated with a positive peak in $\partial\Phi_{-uv}/\partial y$. From the spectra, is it clear that LSM and VLSM exist and are associated with accelerations. This momentum source zone increases in intensity with increasing δ^+ while extending both radially towards the centre of the pipe and also into the lower wavelengths as seen in the $\delta^+ \approx 1000$ and 2000 cases. Our limited δ^+ range suggests that the lower end of region E is limited to about $\lambda_x \approx 3000$, which seems to be the upper bound of the 'inner hump' in the $-uv$ co-spectra.

The intensity of region F in the outer region ($y^+ > 0.5\delta^+$) seems to diminish in strength as a momentum sink with increasing δ^+, and at $\delta^+ \approx 2000$ one can notice the onset of a momentum source. The contribution of $\langle -w\omega_y \rangle^+$ (figure 4, right column) increases in the very outer region of the flow with Reynolds number (albeit weakly), therefore leading to this observation. The main effects underlying these observations are likely to be associated with the weakening negative Reynolds stress gradient (under inner normalisation) with increasing Reynolds number. Another hypothesis could be the effects of the VLSM in E, whereby there is momentum transfer from E to F. Now with a better understanding of regions A, B, C and D, it would appear that A, C and D are part of a larger momentum sink region (figure 4*c*,*e*,*g*); the discontinuity of this large momentum sink as seen in B is due to a strong momentum source (figure 4*d*,*f*,*h*).

Note that in figure 8 (right column) we have also included a black dashed vertical line at $y^+ = y_m^+$, or where the integral of $\partial\Phi_{-uv}^+/\partial y^+$ over all the wavelengths is zero (i.e. the accelerating and the decelerating motions cancel each other). The location of the line suggests that at lower δ^+ the small-scale acceleration (region B) cancels the larger-scale deceleration (region D), whereas at higher δ^+ it is the largest-scale acceleration (region E) that counteracts the relatively smaller-scale deceleration (in regions D and C). It is the growth of the large-scale accelerating motions (region E) that underlies the properties associated with the peak in the Reynolds shear stress. From the previous section, it is evident that the LSM is associated with the change in scale of the eddies.

3.3. *Effect of small and large scales on the mean momentum balance*

Analysis of the co-spectra underlying the TI term allows one to investigate the effects and contributions of the motions at small and large scales (SS and LS) on (1.3) using (2.4). To do this, a suitable cut-off wavelength (λ_c^+) is chosen to segregate the scales of motion characteristic of the contributions to the near-wall peak in the co-spectra of uv from those of much larger scale.

From figure 8 (left column), a cut-off wavelength of $\lambda_c^+ = 3000$ (shown as a black dashed line) is seen to nominally segregate the large scales from the small scales over the present Reynolds-number range. Note that the location of this 'inner hump' in the Reynolds shear stress co-spectra is observed to be invariant (for our δ^+ range) under inner normalisation. Thus, for the present purpose, we adopt this threshold to

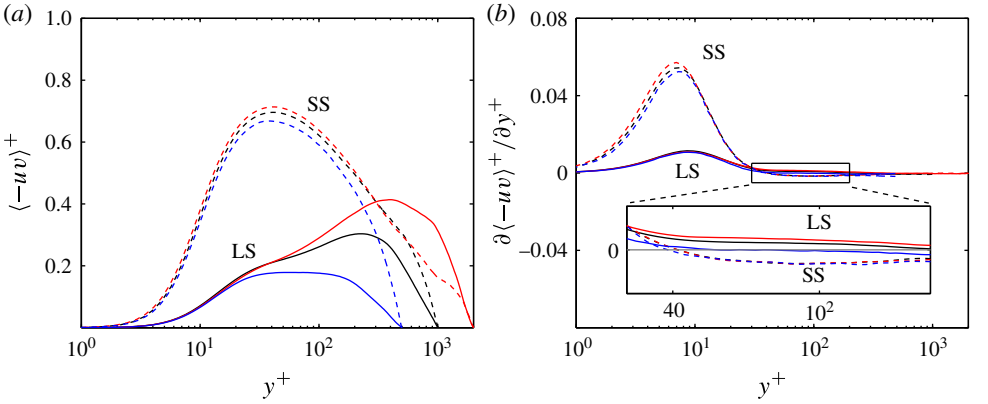

FIGURE 9. (Colour online) Effects and contribution of SS and LS to the (*a*) $\langle -uv \rangle^+$ and (*b*) TI for Reynolds number $\delta^+ \approx 500$ (blue), 1000 (black) and 2000 (red) using a cut-off wavelength of $\lambda_c^+ = 3000$. Dashed lines correspond to SS ($\lambda_x^+ < \lambda_c^+$) and solid lines are for LS ($\lambda_x^+ > \lambda_c^+$).

demarcate LS and SS. (We suspect that a more refined cut-off wavelength is probably required when considering a wider range of Reynolds number.)

The current DNS datasets allow the influences of the SS and LS motion to be quantified as a function of Reynolds number, via the decomposition of (2.4). Figure 9 shows the effects and contributions to the Reynolds stress and the TI. Note that, at any given y^+, the value of the TI term is essentially the integration of figure 8 (right column) across the entire wavelength, λ_x^+, range. Figure 9 shows the decomposition for the chosen cut-off wavelength of $\lambda_c^+ = 3000$, which, while large, is fixed in viscous units. The coloured lines correspond to $\delta^+ \approx 500$ (blue), 1000 (black) and 2000 (red). The dashed lines correspond to the SS contributions and the solid lines are for the LS contributions. Figure 9(*a*) shows that profiles of the SS contribution to $\langle -uv \rangle^+$ remain similar for all δ^+, with only a slight increase in the near-wall peak value. It is apparent that the LS contribution begins to increase with Reynolds number at wall-normal distances beyond $y^+ = 20$. It is interesting to note that for the $\delta^+ \approx 2000$ data the LS contribution becomes greater than the SS contribution above $y^+ \approx 300$ ($y = 0.15\delta$), achieving a peak relative contribution of 65 % at $y^+ \approx 1000$ ($y = 0.5\delta$). This is qualitatively distinct from the lower δ^+ cases, where the SS contribution everywhere exceeds the LS contribution. The LS contribution remains greater up to a wall-normal location of $y^+ \approx 1800$ ($y = 0.9\delta$), which agrees with the findings of Guala *et al.* (2006) at similar Reynolds numbers. Above this wall-normal location, the LS contribution begins to decrease gradually to approximately 35 % at the pipe centre. The effect of λ_c^+ was explored (not presented here) by comparing with an analysis that employed $\lambda_c^+ = 3\delta^+$. (Note that, for $\delta^+ \approx 1000$, $\lambda_c^+ = 3000$ is identical to $\lambda_c^+ = 3\delta^+$.) For $\lambda_c^+ = 3\delta^+$, the LS contribution is consistently less than the SS contribution for all wall-normal locations.

The overall contributions to $\langle uv \rangle^+$ (found by integrating from the wall to the centre) from the SS and LS components for both λ_c^+ are summarised in table 2. Results for $\lambda_c^+ = 3\delta^+$ show that the ratio of SS to LS contribution remains very similar for all Reynolds numbers considered in this study. These results agree with the pipe flow DNS findings of Wu *et al.* (2012) at $\delta^+ \approx 685$. They reported that the SS contribution is 65 %, and the LS contribution is 35 %.

δ^+	SS $(\lambda_x^+ < 3\delta^+)$	LS $(\lambda_x^+ > 3\delta^+)$	SS $(\lambda_x^+ < 3000)$	LS $(\lambda_x^+ > 3000)$
500	0.61	0.39	0.78	0.22
1002	0.64	0.36	0.64	0.36
2003	0.65	0.35	0.47	0.53

TABLE 2. Average contribution of SS and LS to the Reynolds stress $\langle -uv \rangle^+$ using cut-off wavelengths scaled with viscous length scale and δ at $\lambda_c^+ = 3000$ and $3\delta^+$ at different δ^+.

At first glance it might appear that, above the near-wall region, the SS and LS contributions to the TI term merge onto a single profile. Close examination in the region $20 < y^+ < 200$ (see insert of figure 9*b*), however, clearly reveals variations with δ^+. For all δ^+, the SS profiles cross the abscissa at $y^+ \approx 45$. For the LS profiles, the crossing of the abscissa moves to increasing y^+ with increasing δ^+. Recall, in figure 3(*b*), that the zero crossing of the TI increases with Reynolds number as mentioned in figure 4(*b*). Since the SS profiles remain approximately invariant with δ^+, the LS contribution is identified as having a primary association with this zero crossing at increasing y^+. A further investigation of the LS and SS contributions under the decomposition of (2.2) was also performed with a similar cut-off wavelength as in figure 9 (not shown here). It essentially reveals a similar conclusion (to that obtained with reference to figure 4) that, close to y_m^+, the $\langle -w\omega_y \rangle^+$ term is dominated by larger-scale motions with increasing δ^+, while the LS and SS contributions to the $\langle v\omega_z \rangle^+$ term are nearly invariant over the present δ^+ range. Also note that, under the fixed viscous cut-off employed, the SS profiles (in figure 9*a*) show a Reynolds-number dependence near the wall in accordance with the near-wall variation in $\langle -w\omega_y \rangle^+$ (cf. figure 4*b*).

3.4. *Implications regarding the logarithmic region*

The region where $U^+(y^+)$ is logarithmic is often reasoned to constitute an inertial sublayer in physical space (e.g. Tennekes & Lumley 1972). Dynamically, this implies that the VF is negligible compared to the PG and TI, i.e. the leading-order balance is between the first and the third terms of (1.3). Analysis of (1.3) reveals that the inertial domain is bounded from below by $y^+ \approx 2.6\sqrt{\delta^+}$ (e.g. Wei *et al.* 2005). It is now well established (both empirically and via analysis of the mean momentum equation) that the zero crossing of the TI term (or the peak location of the Reynolds shear stress, y_m^+) moves outwards in y^+ like $\sqrt{\delta^+}$ (cf. figure 2). The $\sqrt{\delta^+}$ variation of the lower bound of an inertial logarithmic region is directly coupled to the position, y_m^+. The present results further clarify the physics that underlie this behaviour, and through (2.1) connect these physics to the structure of (1.3).

The zero crossing of the TI term coincides with an exact balance between the $\langle v\omega_z \rangle$ and $\langle w\omega_y \rangle$ contributions to (2.1), with $|\langle w\omega_y \rangle|$ exceeding $|\langle v\omega_z \rangle|$ for $y < y_m$, and $|\langle v\omega_z \rangle|$ exceeding $|\langle w\omega_y \rangle|$ for $y > y_m$. Physically, this indicates that logarithmic dependence is predominantly characterised by the advective dispersion of vorticity, coincident with a diminishing influence of vorticity stretching with increasing y. Conversely, for decreasing y interior to y_m, the vorticity stretching contributions increasingly exceed those of advective transport. This coincides with the leading order balance between the VF and TI terms in layer II. The physical picture here is that (on average) instantaneous viscous forces are amplified because of the intensification of vorticity in the vicinity of stretched vortex cores.

Since the movement of y_m^+ (or the zero crossing of TI) is due to the balance between the terms $\langle v\omega_z\rangle$ (vorticity dispersion) and $\langle -w\omega_y\rangle$ (vorticity stretching), and $\langle v\omega_z\rangle$ exhibits approximate invariance with δ^+ (at least for the present flows, cf. figure 4*a*), it is surmised that $\langle -w\omega_y\rangle$ predominantly dictates the movement of y_m^+. The spectral analysis of $w\omega_y$ (cf. figure 4*d*,*f*,*h*) shows that $\langle -w\omega_y\rangle$ increases with δ^+ due to contributions from motions with primarily streamwise length scales of $O(\delta)$, situated at the wall-normal location near y_m^+. Concretely, $w\omega_y$ motions of scale $\lambda_x \approx O(\delta)$ gain a spectrum of larger length scales with increasing Reynolds number. These results suggest that the beginning of the log region moves out in y^+ owing to vorticity stretching imposed upon the region interior to y_m^+ at $O(\delta)$ wavelengths. Since the near-wall velocity is amplified and modulated by the log region large-scale structures of $O(\delta)$ (e.g. Marusic *et al.* 2010), it is rational to conjecture that the movement of the beginning of the log region (or y_m^+) is associated with the large-scale log region motions changing the length scale of the smaller motions below the log region.

Note that, even though the vorticity stretching underlies the outward migration of the beginning of the log region (in viscous units), it is the vorticity dispersion mechanism that characterises the log region (cf. figure 5). The analysis of Fife *et al.* (2009) reveals that the length scale distribution that describes the mean size of the inertial motions in the logarithmic region asymptotically approaches a linear function. This, along with other attributes of the underlying analysis, reveals a strong correspondence between the similarity structure admitted by (1.3) and Townsend's attached eddy phenomenology where the length scale of the eddies scales linearly with distance from the wall (e.g. Townsend 1976; Perry & Chong 1982; Perry & Marusic 1995). The increasing dominance of the $\langle v\omega_z\rangle$ contribution to TI in the log layer further reinforces this connection, as the Biot–Savart basis from which the attached eddy model reconstructs the statistical structure of the flow requires sufficiently weak nonlinear mechanisms associated with vorticity stretching.

One may also consider the lower bound of the log region using a variant of the above discussion, in terms of eddies and the scaling arguments in a manner similar to those given by Tennekes & Lumley (1972) and Long & Chen (1981). We recall that the outward movement of the beginning of the log region like $\sqrt{\delta^+}$ is derived by Wei *et al.* (2005) from (1.3) by considering that inertially dominated mean flow (log region) is situated beyond where the three terms in (1.3) are of equal order of magnitude (see figure 1*b*). Let us call this wall-normal location δ_m, which is $O(y_m)$. To see the Reynolds-number effect on this location, note that the time scale over which the viscous influence is observed is $\sim\delta_m^2/\nu$, whereas the time scale of an eddy of length scale l (and velocity scale u_τ) is $\sim l/u_\tau$. Larger eddies produce longer time scales, and the longest time scale is due to eddies of size $l \approx \delta$. Therefore, the longest time over which viscosity can affect the eddies is $\delta_m^2/\nu \sim \delta/u_\tau$, which implies that viscous effects can have influence up to the location $\delta_m^+ \sim \sqrt{\delta^+}$. (This is similar to the set of arguments used to describe the Taylor microscale or viscous diffusion in general (e.g. Tennekes & Lumley 1972).) Note that, with increasing δ^+, the viscous time scale does not change (under inner normalisation), while the time scale of the largest eddies increases. It is this longer time at higher δ^+ that allows the viscous effect to penetrate further (in viscous units) from the wall. This is consistent with viscosity only affecting the vorticity stretching part of $\mathrm{d}\langle -uv\rangle^+/\mathrm{d}y^+$ (which is dominant in the near-wall region), and as shown herein it is the large-scale vorticity stretching part that correlates with $y_m^+ \sim \sqrt{\delta^+}$. Note that the eddy argument (within the attached eddy hypothesis) also suggests that both the mean flow and the variances will be affected by viscosity as described. This is consistent with recent data (e.g. Marusic *et al.* 2013;

Sillero, Jiménez & Moser 2013; Vincenti *et al.* 2013), indicating that the beginning of the logarithmic distribution of u^2_{rms} also moves outwards in viscous units like $\sqrt{\delta^+}$.

In this context, the energetic superstructures exist between the regions of concentrated vorticity (Meinhart & Adrian 1995). Consistent with the advective transport mechanism, the spectral analyses of Morrill-Winter & Klewicki (2013) reveal that in the logarithmic region there is an increasing scale separation between v and ω_z, and that the correlation length between v and ω_z becomes approximately invariant for $y^+ \leqslant 40$ when it is normalised by $\sqrt{\delta^+}$ and plotted against $y^+/\sqrt{\delta^+}$. These results suggest that the onset of the advective transport domain (i.e. the logarithmic layer) is likely to depend on a sufficiently three-dimensionalised vorticity field whose characteristic motions have also attained a sufficient level of scale separation from the motions characteristic of the velocity field. The present results substantively augment these findings by revealing that the $\sqrt{\delta^+}$ dependence of the beginning of the advective domain results from scale changes of the eddy structure. Collectively, the emerging picture is one in which the $O(\delta)$ log layer superstructures energetically perturb the near-wall vorticity field, and this vorticity field responds at a scale that is $O(\sqrt{\nu\delta/u_\tau})$.

4. Summary and conclusions

The TI term, which is the wall-normal gradient of Reynolds shear stress in the axial mean momentum equation for a turbulent pipe flow, has been analysed using two different decompositions in spectral form: (i) the velocity–vorticity decomposition of (2.1) and (ii) the force spectrum decomposition of (2.4), across three different Reynolds numbers, $\delta^+ \approx 500$, 1000 and 2000.

Our main purposes are (i) to better understand how the turbulent motions at different length scales influence the balance of terms in (1.3) via changes in TI, and draw further connections between the conceptual picture of turbulent wall flows in terms of coherent motions (occurring over a range of scales) and the governing mean equation, and (ii) to construct a cogent physical description for why the zero crossing of TI scales like $y^+_m \sim \sqrt{\delta^+}$ (cf. figure 2), and how this physically connects to the onset of the log region, for which existing evidence also supports an inner-normalised lower bound scaling with $\sqrt{\delta^+}$.

In the velocity–vorticity decomposition, TI is written as the sum of $\langle v\omega_z\rangle$ and $\langle -w\omega_y\rangle$. These two contributions are respectively associated with the physical mechanisms of advective transport (vorticity dispersion) and changes in scale (vorticity stretching). For all Reynolds numbers, close to the wall (below y^+_m) $\langle -w\omega_y\rangle$ provides a more significant contribution to TI than $\langle v\omega_z\rangle$, whereas above y^+_m the roles are reversed. (At y^+_m the two terms are identically equal.) With increasing δ^+ the location of balance, y^+_m, increases. Very close to the wall (below $y^+ \approx 10$) $\langle v\omega_z\rangle$ is positive and then becomes negative above $y^+ \approx 10$. A weighted joint p.d.f. of v and ω_z below and above $y^+ \approx 10$ shows that the near-wall positive behaviour of $\langle v\omega_z\rangle$ arises primarily because of $[+]\,v$ and $[+]\,\omega_z$, whereas the further negative behaviour largely stems from $[+]\,v$ and $[-]\,\omega_z$. These behaviours suggest connections to coherent motions as discussed further below in § 4.1. The $\langle -w\omega_y\rangle$ term, however, remains positively signed approximately below the lower bound of the log region and for greater wall-normal distances becomes negative. With increasing δ^+, the distribution of $\langle v\omega_z\rangle^+$ is approximately invariant. This is somewhat surprising, since this term is not dominant near the wall, whereas $\langle -w\omega_y\rangle$ shows variations with δ^+ in viscous scaling, even though it has a greater contribution to TI close to the wall.

Streamwise spectral decompositions of $v\omega_z$ and $w\omega_y$ (for various y locations) show that for $v\omega_z$ the peak in the pre-multiplied co-spectra (of v and ω_z, $\Phi_{v\omega_z}$) occurs at a length scale of $\lambda_x^+ \approx 500$–700 and when scaled in inner units $\Phi_{v\omega_z}$ is approximately invariant with δ^+. The pre-multiplied co-spectrogram (of $-w$ and ω_y, $\Phi_{-w\omega_y}$), however, shows noticeable variations with δ^+. Importantly, these variations are at $O(\delta^+)$ wavelengths in the region close to y_m^+. In this regard, the location of y_m^+ (and the associated beginning of the log region, the outer edge of layer III) faithfully tracks the large-scale variation in $\Phi_{-w\omega_y}$ with changing Reynolds number (cf. figure 4*d*,*f*,*h*).

In the second decomposition, the TI term is represented in the form of the force spectrum, $\partial\Phi_{-uv}/\partial y$ (the wall-normal gradient of the co-spectrum of u and v), which has been used by Adrian and co-workers to understand the influence of acceleration ($[+]\,\partial\Phi_{-uv}/\partial y$) and deceleration ($[-]\,\partial\Phi_{-uv}/\partial y$) caused by turbulence related to different length scales of coherent motions (commonly observed in turbulent boundary layers). Note that, evidently, $\partial\Phi_{-uv}/\partial y = \Phi_{v\omega_z} + \Phi_{-w\omega_y}$. Therefore, this allows the acceleration and deceleration effects of turbulence to be connected to mechanisms associated with the velocity vorticity products (in terms of effects due to vorticity dispersion and vorticity stretching).

When plotted as contours on a y^+ versus λ_x^+ graph, the inner-normalised force spectrum for small y^+ ($\lesssim 5$) and independent of λ_x^+, and at smaller λ_x^+ ($\lesssim 300$) and independent of y^+, is invariant with Reynolds number. The $y^+ \lesssim 5$ region is always associated with accelerations owing to the same signed contributions from $\Phi_{v\omega_z}$ and $\Phi_{-w\omega_y}$. For the $\lambda_x^+ \lesssim 300$ region, however, there are alternating accelerating and decelerating regions with changing y^+ because $\Phi_{v\omega_z}$ switches sign. This is primarily related to ω_z changing sign. The main variation with Reynolds number is observed to come from large λ_x^+ motions, and above $\approx y_m^+$. Here the motions are associated with strong accelerations. With increasing δ^+ this large-scale accelerative effect influences the smaller scales, and thus connects to the emergence of a secondary peak in the co-spectrogram of u and v, Φ_{-uv}, that is located in the log region at large wavelengths (cf. figure 8, left column).

At lower Reynolds numbers, the location of y_m^+ (where the integral of $\partial\Phi_{-uv}/\partial y$ over all λ_x^+ is equal to zero) is realised through the balance of accelerating motions at smaller wavelengths ($\lambda_x^+ \lesssim 300$) and decelerating motions at larger wavelengths ($\lambda_x^+ \approx \delta^+$). With increasing Reynolds number, y_m^+ increases owing to a shift in the balance to that between decelerating motions at larger wavelengths $\lambda_x^+ \approx \delta^+$ and accelerating motions at very large wavelengths ($\lambda_x^+ \approx 10\delta^+$). The velocity–vorticity decomposition reveals that these very-large-wavelength accelerating motions are associated with scale changes in the relevant eddy structure. Furthermore, by splitting TI into small- and large-scale contributions, it was evidenced that these large-scale features underlie the outward movement of y_m^+ with increasing Reynolds number.

4.1. *Further physical interpretation*

Given the quantitative results for TI decompositions into $\langle v\omega_z\rangle$ and $\langle -w\omega_y\rangle$, and $\partial\Phi_{-uv}/\partial y$, it is of value to consider further possible physical interpretations of these results. Our interpretations begin by dividing the turbulent wall flow into two regions, below y_m^+ and above it. This dividing line approximately coincides with the onset of the logarithmic region.

Within the domain below y_m^+, flow visualisations and particle image velocimetry studies indicate that very close to the wall ($y^+ \lesssim 5$) the sublayer streaks exist, above which one can observe hairpin or lambda vortices (where heads of hairpin

vortices correspond to $\approx [-]\,\omega_z$). These motions are evidenced to often combine to form packets of hairpin vortices (e.g. Adrian 2007; Adrian & Marusic 2012). This has long been recognised as a region of intense turbulence. The significance of the change-of-scale effect ($\langle -w\omega_y \rangle$) over advective transport ($\langle v\omega_z \rangle$) is consistent with this region being characterised by intense vorticity stretching and reorientation, leading to the rapid three-dimensionalisation of the vorticity field with increasing y^+ (Klewicki 2013*a*). The $[+]\,v$ and $[+]\,\omega_z$ below $y^+ \lesssim 5$ are an indication of the low-speed sublayer streaks lifting up, whereas $[+]\,v$ and $[-]\,\omega_z$ are consistent with the hairpin vortex paradigm (Zhou *et al.* 1999; Adrian *et al.* 2000). The force spectrum analysis suggests associating the sublayer streaks with regions of large acceleration, whereas the smaller-scale alternating acceleration and deceleration can be associated with the complex hairpin packet organisation process that is prevalent below y_m^+.

Above y_m^+ in the log region and beyond, the vortical motions are known to be of a size that shows little variation (e.g. Klewicki & Falco 1996; Carlier & Stanislas 2005; Wu & Christensen 2006). This suggests that, once vortices are formed interior to y_m^+, they are largely advected away, similar to a passive scalar dispersed in turbulence (e.g. Elsinga *et al.* 2012), but not wholly (Klewicki 2013*a*). The present results support this picture, where we observe the significance of $\langle v\omega_z \rangle$ (advective dispersion) over $\langle -w\omega_y \rangle$ (change of scale) above y_m^+. The seemingly surprising fact that the $\langle v\omega_z \rangle^+$ profile remains essentially invariant reinforces a picture in which the vortices that form below y_m^+ are then advected above y_m^+. Furthermore, the modulation (change of length scale) of the near-wall motions by the $O(\delta^+)$ log region VLSM/superstructures (Hutchins & Marusic 2007; Marusic *et al.* 2010) provides a self-consistent mechanism for the variation in $\langle -w\omega_y \rangle^+$ with δ^+. It is thus suggested that this variation in $\langle -w\omega_y \rangle$, as induced by contributions from the superstructures, results in the location of y_m^+ to move outwards with increasing δ^+. This description of why $y_m^+ \sim \sqrt{\delta^+}$ was shown to be consistent with $O(\delta^+)$ superstructures (situated near the lower edge of the logarithmic layer) setting the time scale over which viscous influences can act. The classical scaling argument (by equating the time scale of viscous influence to reach y_m^+ with the time allowed by the largest eddy, δ/u_τ) then leads one to conclude that the y^+ domain where the viscous influence remains of leading order will move outwards like $\sqrt{\delta^+}$, and thus the onset of the logarithmic layer will do so as well.

We understand that the $\sqrt{\delta^+}$ scaling of the onset of the log region deviates from the classical two-layer theory of wall turbulence and challenges the orthodoxy. However, there is now sufficient evidence from theory and both DNS as well as high-Reynolds-number experiments that make the deviations from the classical theory compelling. In the present paper, we have provided a plausible physical mechanism for the $\sqrt{\delta^+}$ scaling. No doubt, a truly definitive conclusion on the log region scaling will require further physical probing and invariably higher-Reynolds-number experiments (which unfortunately are not foreseeable in the near to medium-range time frame).

The present results are derived from the analysis of turbulent pipe flow. However, the movement of the lower bound of the log region is observed by Marusic *et al.* (2013) to be relevant for boundary layers as well, and the four-layer structure (presented in figure 1) is also shown by Wei *et al.* (2005), Metzger, Lyons & Fife (2008) and Klewicki (2013*b*) to be valid in channel and boundary layers too (with slight differences due to the PG term being replaced by mean advection). Therefore, the present physical arguments regarding the movement of y_m^+ and the associated movement of the lower bound of the log region are also likely to hold generically for boundary layers and channels as well.

We lastly note that the present findings have potential implications regarding flow control. Herein it was observed that, with increasing Reynolds number, the secondary peak in the *uv* co-spectra emerges (at larger wavelengths), and this LSM (associated with flow accelerations) is responsible for increasing the length scale of eddies closer to the wall. In this respect, controlling the LSM presents a potentially feasible option for flow control.

Acknowledgements

This research was undertaken with the assistance of resources provided at the National Computational Infrastructure National Facility (NCI NF) through the National Computational Merit Allocation Scheme supported by the Australian Government. This research was supported by a Victorian Life Sciences Computation Initiative (VLSCI) grant number VR0057 at its Peak Computing Facility at the University of Melbourne, an initiative of the Victorian Government, Australia. The authors also acknowledge the financial support of the Australian Research Council.

REFERENCES

ABE, H., KAWAMURA, H. & MATSUO, Y. 2001 Direct numerical simulation of a fully developed turbulent channel flow with respect to the Reynolds number dependence. *Trans. ASME: J. Fluids Engng* **123**, 382–393.

ADRIAN, R. J. 2007 Hairpin vortex organization in wall turbulence. *Phys. Fluids* **19**, 041301.

ADRIAN, R. J. & MARUSIC, I. 2012 Coherent structures in flow over hydraulic engineering surfaces. *J. Hydraul Res.* **50**, 451–464.

ADRIAN, R. J., MEINHART, C. D. & TOMKINS, C. D. 2000 Vortex organization in the outer region of the turbulent boundary layer. *J. Fluid Mech.* **422**, 1–54.

AFZAL, N. 1982 Fully developed turbulent flow in a pipe: an intermediate layer. *Ing.-Arch.* **52**, 355–377.

DEL ÁLAMO, J. C. & JIMÉNEZ, J. 2003 Spectra of the very large anisotropic scales in turbulent channels. *Phys. Fluids* **15**, L41–L44.

DEL ÁLAMO, J. C., JIMÉNEZ, J., ZANDONADE, P. & MOSER, R. D. 2004 Scaling of the energy spectra of turbulent channels. *J. Fluid Mech.* **500**, 135–144.

BALAKUMAR, B. J. & ADRIAN, R. J. 2007 Large- and very-large-scale motions in channel and boundary-layer flows. *Phil. Trans. R. Soc. Lond.* A **365**, 665–681.

BERNARD, P. S. & HANDLER, R. A. 1990 Reynolds stress and the physics of turbulent momentum transport. *J. Fluid Mech.* **220**, 99–124.

BUSCHMANN, M. H., INDINGER, T. & GAD-EL-HAK, M. 2009 Near-wall behavior of turbulent wall-bounded flows. *Intl J. Heat Fluid Flow* **30**, 993–1006.

CARLIER, J. & STANISLAS, M. 2005 Experimental study of eddy structures in a turbulent boundary layer using particle image velocimetry. *J. Fluid Mech.* **535**, 143–188.

CHIN, C., MONTY, J. P. & OOI, A. 2014 Reynolds number effects in DNS of pipe flow and comparison with channels and boundary layers. *Intl J. Heat Fluid Flow* **45**, 33–40.

CHIN, C., OOI, A., MARUSIC, I. & BLACKBURN, H. M. 2010 The influence of pipe length on turbulence statistics computed from DNS data. *Phys. Fluids* **22**, 115107.

DEGRAAFF, D. B. & EATON, J. K. 2000 Reynolds number scaling of the flat-plate turbulent boundary layer. *J. Fluid Mech.* **422**, 319–346.

DENNIS, D. J. C. & NICKELS, T. B. 2011 Experimental measurement of large-scale three-dimensional structures in a turbulent boundary layer. Part 2. Long structures. *J. Fluid Mech.* **673**, 218–244.

ELSINGA, G. E., POELMA, C., SCHRODER, A., GEISLER, R., SCARANO, F. & WESTERWEEL, J. 2012 Tracking of vortices in a turbulent boundary layer. *J. Fluid Mech.* **697**, 143–188.

EYINK, G. L. 2008 Turbulent flow in pipes and channels as cross-stream inverse cascades of vorticity. *Phys. Fluids* **20**, 125101.

FIFE, P., KLEWICKI, J. & WEI, T. 2009 Time averaging in turbulence settings may reveal an infinite hierarchy of length scales. *J. Discrete Continuous Dyn. Syst.* **24**, 781–807.

GUALA, M., HOMMEMA, S. E. & ADRIAN, R. J. 2006 Large-scale and very-large-scale motions in turbulent pipe flow. *J. Fluid Mech.* **554**, 521–542.

HULTMARK, M., VALLIKIVI, M., BAILEY, S. C. C. & SMITS, A. J. 2013 Logarithmic scaling of turbulence in smooth- and rough-wall pipe flow. *J. Fluid Mech.* **728**, 376–395.

HUTCHINS, N. & MARUSIC, I. 2007 Evidence of very long meandering features in the logarithmic region of turbulent boundary layers. *J. Fluid Mech.* **579**, 1–28.

KIM, K. C. & ADRIAN, R. J. 1999 Very large-scale motion in the outer layer. *Phys. Fluids* **11** (2), 417–422.

KLEWICKI, J. C. 1989 Velocity–vorticity correlations related to the gradients of the Reynolds stresses in parallel turbulent wall flows. *Phys. Fluids* A **1**, 1285–1288.

KLEWICKI, J. C. 2010 Reynolds number dependence, scaling, and dynamics of turbulent boundary layers. *Trans. ASME: J. Fluids Engng* **9**, 094001.

KLEWICKI, J. 2013*a* A description of turbulent wall-flow vorticity consistent with mean dynamics. *J. Fluid Mech.* **737**, 176–204.

KLEWICKI, J. 2013*b* Self-similar mean dynamics in turbulent wall-flows. *J. Fluid Mech.* **718**, 596–621.

KLEWICKI, J., CHIN, C., BLACKBURN, H. M., OOI, A. & MARUSIC, I. 2012 Emergence of the four layer dynamical regime in turbulent pipe flow. *Phys. Fluids* **24** (4), 045107.

KLEWICKI, J. C. & FALCO, R. E. 1996 Spanwise vorticity structure in turbulent boundary layers. *Intl J. Heat Fluid Flow* **17**, 363–376.

KLEWICKI, J., FIFE, P., WEI, T. & MCMURTRY, P. 2007 A physical model of the turbulent boundary layer consonant with mean momentum balance structure. *Phil. Trans. R. Soc. Lond.* A **365**, 823–839.

KLEWICKI, J. & HIRSCHI, C. R. 2004 Flow field properties local to near-wall shear layers in a low Reynolds number turbulent boundary layer. *Phys. Fluids* **16**, 4163–4176.

KLEWICKI, J., MURRAY, J. A. & FALCO, R. E. 1995 Vortical motion contributions to stress transport in turbulent boundary layers. *Phys. Fluids* **6**, 277–286.

KLINE, S. J., REYNOLDS, W. C., SCHRAUB, F. A. & RUNSTANDLER, P. W. 1967 The structure of turbulent boundary layer. *J. Fluid Mech.* **30**, 741–773.

LEE, J. H. & SUNG, H. J. 2013 Comparison of very-large-scale motions of turbulent pipe and boundary layer simulations. *Phys. Fluids* **25**, 045103.

LONG, R. R. & CHEN, T. C. 1981 Experimental evidence for the existence of the mesolayer in turbulent systems. *J. Fluid Mech.* **105**, 19–59.

MARUSIC, I. 2001 On the role of large-scale structures in wall turbulence. *Phys. Fluids* **13** (3), 735–743.

MARUSIC, I., MATHIS, R. & HUTCHINS, N. 2010 A predictive inner–outer model for streamwise turbulence statistics in wall-bounded flows. *Science* **329**, 193–196.

MARUSIC, I., MONTY, J. P., HULTMARK, M. & SMITS, A. J. 2013 On the logarithmic region in wall turbulence. *J. Fluid Mech.* **716**, R3.

MATHIS, R., MONTY, J. P., HUTCHINS, N. & MARUSIC, I. 2009 Comparison of large-scale amplitude modulation in turbulent boundary layers, pipes, and channel flows. *Phys. Fluids* **21**, 111703.

MEINHART, C. D. & ADRIAN, R. J. 1995 On the existence of uniform momentum zones in a turbulent boundary layer. *Phys. Fluids* **7**, 694.

METZGER, M., LYONS, A. & FIFE, P. 2008 Mean momentum balance in moderately favourable pressure gradient turbulent boundary layers. *J. Fluid Mech.* **617**, 107–140.

MONTY, J. P., STEWART, J. A., WILLIAMS, R. C. & CHONG, M. S. 2007 Large-scale features in turbulent pipe and channel flows. *J. Fluid Mech.* **589**, 147–156.

MORRILL-WINTER, C. & KLEWICKI, J. 2013 Influences of boundary layer scale separation on the vorticity transport contribution to turbulent inertia. *Phys. Fluids* **24**, 015108.

PERRY, A. E. & CHONG, M. S. 1982 On the mechanism of wall turbulence. *J. Fluid Mech.* **119**, 173–217.

PERRY, A. E. & MARUSIC, I. 1995 A wall-wake model for the turbulence structure of boundary layers. Part 1. Extension of the attached eddy hypothesis. *J. Fluid Mech.* **298**, 361–388.

ROBINSON, S. K. 1991 Coherent motions in the turbulent boundary layer. *Annu. Rev. Fluid Mech.* **23**, 601–639.

SILLERO, J. A., JIMÉNEZ, J. & MOSER, R. D. 2013 One-point statistics for turbulent wall-bounded flows at Reynolds numbers up to $\delta^+ = 2000$. *Phys. Fluids* **25**, 105102.

SREENIVASAN, K. R. 1989 The turbulent boundary layer. In *Frontiers in Experimental Fluid Mechanics*, pp. 159–209. Springer.

SREENIVASAN, K. R. & SAHAY, A. 1997 The persistence of viscous effects in the overlap region, and the mean velocity in turbulent pipe and channel flows. *Adv. Fluid Mech.* **15**, 253–272.

TAYLOR, G. I. 1932 The transport of vorticity and heat through fluids in turbulent motion. *Proc. R. Soc. Lond.* A **135**, 685–702.

TENNEKES, H. & LUMLEY, J. L. 1972 *A First Course in Turbulence*. MIT Press.

TOWNSEND, A. A. 1976 *The Structure of Turbulent Shear Flow*. *(*vol. 2), Cambridge University Press.

TOWNSEND, A. A. 1987 Organized eddy structures in turbulent flows. *Physico-Chem. Hydrodyn.* **8**, 23–30.

VINCENTI, P., KLEWICKI, J., MORRILL-WINTER, C., WHITE, C. & WOSNIK, M. 2013 Streamwise velocity statistics in turbulent boundary layers that spatially develop to high Reynolds number. *Exp. Fluids* **54**, 1629.

WALLACE, J. M. 1982 On the structure of bounded turbulent shear flow: a personal view. In *Developments in Theoretical and Applied Mechanics* (ed. T. J. Chung & G. R. Karr), vol. XI, pp. 509–521. University of Alabama, Huntsville.

WEI, T., FIFE, P., KLEWICKI, J. & MCMURTRY, P. 2005 Properties of the mean momentum balance in turbulent boundary layer, pipe and channel flows. *J. Fluid Mech.* **522**, 303–327.

WEI, T. & WILLMARTH, W. W. 1989 Reynolds number effects on the structures of a turbulent channel flow. *J. Fluid Mech.* **204**, 57–95.

WU, X., BALTZER, J. R. & ADRIAN, R. J. 2012 Direct numerical simulation of a $30R$ long turbulent pipe flow at $R^+ = 685$: large- and very large-scale motions. *J. Fluid Mech.* **698**, 235–281.

WU, Y. & CHRISTENSEN, K. T. 2006 Population trends of spanwise vortices in wall turbulence. *J. Fluid Mech.* **568**, 55–76.

ZHOU, J., ADRIAN, R. J., BALACHANDAR, S. & KENDALL, T. M. 1999 Mechanisms for generating coherent packets of hairpin vortices in channel flow. *J. Fluid Mech.* **387**, 353–396.